The Journal of Adhesion

ISSN: (Print) (Online) Journal homepage: www.tandfonline.com/journals/gadh20

Surface morphology influences on the adhesive bond performance of PBF-LB manufactured Ti6Al4V parts – investigation of quasi-static and fatigue loading conditions

Emre Ertürk, Jörg Gregor Diez, Pablo Vitale & Philipp Höfer

To cite this article: Emre Ertürk, Jörg Gregor Diez, Pablo Vitale & Philipp Höfer (07 Jan 2025): Surface morphology influences on the adhesive bond performance of PBF-LB manufactured Ti6Al4V parts – investigation of quasi-static and fatigue loading conditions, The Journal of Adhesion, DOI: 10.1080/00218464.2024.2441886

To link to this article: https://doi.org/10.1080/00218464.2024.2441886

Published online: 07 Jan 2025.

THE JOURNAL OF ADHESION
https://doi.org/10.1080/00218464.2024.2441886

Taylor & Francis
Taylor & Francis Group

Surface morphology influences on the adhesive bond performance of PBF-LB manufactured Ti6Al4V parts – investigation of quasi-static and fatigue loading conditions

Emre Ertürk, Jörg Gregor Diez, Pablo Vitale, and Philipp Höfer

Institute of Lightweight Engineering, University of the Bundeswehr Munich, Neubiberg, Germany

ABSTRACT

Adhesive bonding of additively manufactured parts enables highly efficient lightweight designs. To achieve high adhesive bond performance, it is essential to consider the surface properties of the adherends. Previous studies have shown that the inherent roughness of Ti6Al4V parts fabricated by laser powder bed fusion (PBF-LB) can contribute to high bond strength under quasi-static loading. In the present work, the influences of surface morphology on adhesive bond performance were examined under static and fatigue loading conditions. Moreover, the environmental durability of the bonded joints was assessed for a hot-wet condition. In the as-built state (i.e. degreased PBF-LB-surface) the build orientations 0°, 45° (Up-/Downskin) and 90° were investigated, resulting in four different surface morphologies. Furthermore, grit blasting and laser treatment were used to modify the surface properties and examine their effect on the adhesive bond performance. Characterizing the surfaces was done by scanning electron microscopy and confocal laser scanning microscopy. The quasi-static bond strengths and fatigue lifetimes were examined through metal-metal single step-lap joint testing. The number of attached particles on the PBF-LB manufactured surfaces was found to correlate with the tensile shear strength and fatigue lifetime of the adhesive bond. Under fatigue loading, the particle-induced interlocking effect was mainly effective in the low-cycle-fatigue regime. A significantly enhanced bond performance was achieved by laser treatment, which created a hierarchical surface morphology, consisting of the inherent microscopic surface features of PBF-LB-Ti6Al4V and a laser-induced nanoporous oxide layer. This hierarchical surface structure increased the bond strengths by up to 162% and extended the fatigue lifetimes by at least 130% in comparison to the as-built surface condition. However, further improvements are necessary to enhance the environmental durability of the oxide layer.

ARTICLE HISTORY
Received 20 October 2024
Accepted 9 December 2024

KEYWORDS
Adhesive bonding; additive manufacturing; surface morphology; surface treatment

CONTACT Emre Ertürk emre.ertuerk@unibw.de Institute of Lightweight Engineering, University of the Bundeswehr Munich, Werner-Heisenberg-Weg 39, Neubiberg 85577, Germany

1. Introduction

Additive manufacturing (AM) enables the fabrication of complex, lightweight components with high design flexibility and structural efficiency. For aerospace applications, the titanium alloy Ti6Al4V is widely used due to its exceptional mechanical and thermal properties. However, despite the remarkable advancements in metal AM, the process still faces challenges, such as the need for effective joining methods to assemble printed parts.[1] In this context, structural adhesive bonding proves to be a suitable joining method for lightweight constructions, as it introduces low-weight penalties compared to mechanical fastening methods, offers enhanced resistance to fatigue and corrosion, and enables an improved load distribution.[2,3] Common failure modes of adhesively bonded joints involve adhesive failure (i.e., interfacial failure) between adherend and adhesive, cohesive failure in the adhesive layer and a combination of both (mixed-mode failure). In structural adhesive joints, adhesive failure is generally considered an unacceptable failure mode since it indicates an insufficient surface preparation.[4] Consequently, it is essential to ensure high adhesion between adherend and adhesive that can endure both quasi-static and fatigue loading conditions, while also maintaining durability under environmental aging influences.

In the case of PBF-LB manufactured Ti6Al4V parts, previous investigations[5–7] have demonstrated that the inherent surface roughness enables high adhesive bond strengths under quasi-static loading conditions. The surface topographies are primarily characterized by a specific quantity of partially melted particles, which varies depending on the build orientation.[6–8] These particles improve adhesive bond performance by increasing the total surface area and promoting mechanical interlocking of the adhesive.[6,7] Ardila-Rodríguez et al.[6] found that PBF-LB-Ti6Al4V surfaces in the as-built condition (i.e., referring to degreased PBFL-LB printed surfaces) exhibit tensile bond strengths comparable to those observed after grit blasting. This result shows the bonding potential of additively manufactured metal surfaces. However, fracture analysis in[6] revealed a significant amount of adhesive failure on these surfaces, indicating insufficient adhesion strength. The main reason for the observed adhesive failure is that the as-built surfaces lack distinct nanoroughness, which can significantly enhance adhesion.[9] The same issue applies to grit blasted surfaces, resulting often in similar mixed-mode failure of the adhesive joint.[6,7] The roughness scales present on the surface, along with the adhesive's capability to penetrate and fill micro- and nanoscale voids are decisive factors for high adhesion strength, as demonstrated in recent studies.[7,10–12] To achieve fully cohesive failure within the adhesive, it is therefore necessary to apply an appropriate surface treatment. In aerospace, the common standard for bonding preparation of metals like titanium or aluminum involves the use of electrochemical methods, such as

phosphoric acid anodizing (PAA)[13] and NaTESi,[14] which generate a pronounced nanoscale roughness on the surface. The main disadvantages of electrochemical treatments are their high process costs and the use of hazardous chemicals, which pose environmental and safety risks. A more sustainable method is laser treatment, which also offers the advantage of high automation. Kurtovic[15] conducted a comprehensive investigation into the effects of laser treatment on conventionally manufactured Ti6Al4V and its influences on adhesive bond performance. By conducting floating roller peel tests and wedge tests Kurtovic showed that a laser-generated nanoroughness can improve adhesion strength compared to wet chemical surface treatments like etching (Turco 5578) or anodizing (NaTESi). In a study by Tseng and Chen[16] laser treatment of conventionally manufactured Ti6Al4V substrates allowed to achieve a threefold increase in tensile shear bond strength compared to the untreated surface condition. Further, for pin-reinforced titanium/CFRP single-lap-shear (SLS) joints, Parkes et al.[17] found that laser treatment improves the consistency of co-bonding and increases the elastic limit of the joint. Regarding PBF-LB-Ti6Al4V surfaces, it was demonstrated in a previous work[7] that a laser-induced nanoporous oxide layer significantly increases tensile bond strength, leading to a shift from mixed-mode failure in the as-built condition to cohesive failure in the epoxy adhesive.

An extensive literature review on the effect of surface texture on adhesive bond performance was conducted by Naat et al.[18] This review highlighted that most research has focused on the effects of surface treatments on quasi-static bond strength, whereas only relatively few works have investigated the influences on fatigue resistance. Consequently, further research is needed to better understand the influence of surface morphology on the fatigue behavior of bonded joints. Barros et al.[19] investigated the effects of grit, sand and bristle blasting on the fatigue performance of steel joints bonded with an epoxy adhesive. Their end-notched flexure (ENF) tests showed that bristle-blasted surfaces, characterized by sharp asperities, exhibited significantly shorter fatigue lifetimes. The detrimental effect of sharp surface features on fatigue resistance was also observed by Thäsler et al.[20] and Morfini et al.[21] for peel-ply structured CFRP/CFRP SLS joints and hand-sanded aluminum/magnesium SLS joints, respectively. Several studies have shown that, compared to mechanical surface treatments, higher fatigue strengths can be achieved through electrochemical anodizing processes and laser treatments, due to the provided superior adhesion strength.[18] Gudladt and Frömmel[22] demonstrated for aluminum SLS joints bonded with a two-part epoxy adhesive that the application of a pulsed Nd:YAG-Laser with optimized settings can create a distinct nanoroughness, which substantially enhances fatigue lifetimes. Improved fatigue performance of aluminum alloy and stainless steel SLS joints was also achieved by Moroni et al.[23] through laser ablation with a Yb-fiber laser. The increased lifetime was strongly related to a prolonged crack

propagation phase. However, at higher laser energy density levels, void formations were observed in the surface valleys, which deteriorated the fatigue performance. Regarding the fatigue resistance of PBF-LB-Ti6Al4V adherends, existing literature primarily focuses on the effects of surface roughness on the fatigue behavior of the bulk Ti6Al4V substrate without adhesive bonding. Studies in[24,25] have shown that Ti6Al4V parts exhibit in as-built condition low fatigue strength due to their high surface roughness, necessitating a surface finishing process. In the case of grit blasted Ti6Al4V parts, Bagehorn et al.[24] reported that incised blasting residues can worsen fatigue performance by causing crack initiation. Furthermore, investigations on laser treated Ti6Al4V surfaces[15,26] have found that the laser process can deteriorate fatigue properties due to the introduction of laser-induced micro- and nanoroughness, surface cracking and tensile residual stresses near the surface. To the authors best knowledge, no studies have yet examined the fatigue behavior of bonded metal/metal joints with PBF-LB-Ti6Al4V substrates for different surface conditions. As shown in,[24,25] the as-built surface roughness of additively manufactured Ti6Al4V leads to low fatigue strengths of the metal substrate. However, the inherent surface roughness may prove advantageous in adhesive bonding, particularly when the surface morphology is further optimized through suitable surface treatments. This is a central aspect of the present work.

Durability under environmental conditions is another critical aspect of structural adhesive bonding and was therefore also considered in this study. A crucial factor influencing the long-term performance of adhesive joints is moisture diffusion into the adhesive, as it affects the mechanical properties of the adhesive and can lead to a reduction in adhesion strength.[27,28] To ensure sufficient adhesion under environmental stresses, surface treatment is often required prior to bonding. While mechanical surface treatments typically result in moderate durability, electrochemical anodizing can produce surfaces with high durability for adhesive bonds.[9,18,29] Regarding the aging behavior of bonded titanium (Ti15–3)-PEEK SLS joints under hot-wet conditions, Löbbecke et al.[30] demonstrated that long-term stable adhesion can be achieved through laser treatment of titanium if an open porous branched nanoroughness layer is formed on the surface. Freund et al.[31] reported that high durability under hot-wet aging was achieved for co-cured AW6082-T6–CFRP SLS joints when the laser treatment created significant surface enlargement, deep craters and undercut structures on the metal substrate. Similarly, hydrothermally stable SLS joints were achieved by Specht et al.[32] through laser treatment of conventionally manufactured Ti6Al4V. For PBF-LB-Ti6Al4V surfaces, it was shown in[6] that salt-spray aging significantly reduces the tensile bond strength in case of the as-built surfaces. However, the durability of the adhesive joint was substantially improved after a combination of sol-gel and primer application.

In this work, the surface morphology influences on the bonding behavior of PBF-LB-Ti6Al4V were investigated for quasi-static and fatigue loading conditions. The as-built condition was analyzed for the build orientations 0°, 45° (up-/downskin) and 90°. Furthermore, the effects of grit blasting and laser treatment on surface morphology and bonding performance were evaluated. Surface characterization was performed using Scanning Electron Microscopy (SEM), Ion Beam Milling (IBM) and Confocal Laser Scanning Microscopy (CLSM). Afterwards, quasi-static bond strengths and fatigue lifetimes were examined through single step-lap joint testing. To assess the environmental durability of the bonded joints, a subset of the specimens was hot-wet aged before quasi-static testing. In addition, Digital Image Correlation (DIC) was employed for strain measurement at the bondline and for monitoring crack growth during the fatigue tests.

2. Materials and methods

2.1. Specimen type and substrate manufacturing

Single step-lap joint (SLJ) specimens made of PBF-LB manufactured Ti6Al4V substrates were used in this study. For bonding, the two-component epoxy adhesive Loctite EA 9396 AERO was utilized. The specimen geometry was defined based on DIN EN 2243–6[33] and is depicted in Figure 1. Single lap joints are subjected to mixed-mode loading, comprising both non-uniform shear and peel stresses. A stepped geometry with thick adherends was used

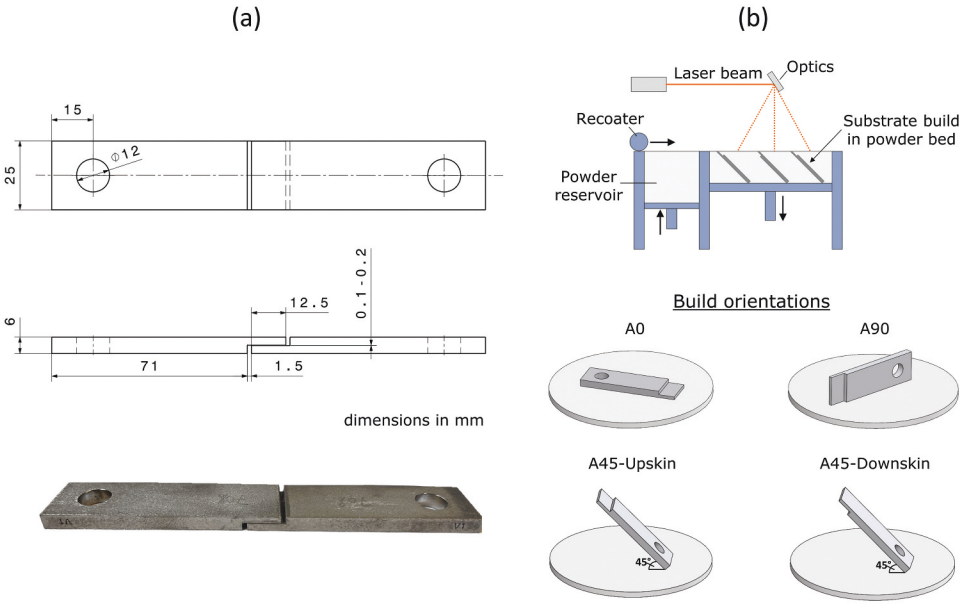

Figure 1. (a) SLJ specimen geometry and (b) substrate build orientations in the PBF-LB/M process.

here to reduce the peel stresses at the overlap ends induced by eccentric loading. This design allowed the investigation of a primarily shear-loaded adhesive joint with reduced peel stresses at the overlap ends. Such a load combination is representative of many technical applications, as adhesive joints are typically designed to minimize high peel stresses,[9] while non-uniform stress distributions, similar to those in this specimen type, are often encountered in practice.

The substrates for the metal-metal SLJ specimens were manufactured using a Trumpf TruPrint 5000 PBF-LB/M printer with standard parameters for Ti6Al4V Grade 23. The printing process utilized a layer thickness of 60 µm and a scanning strategy involving a 45° stripe pattern. To investigate the build orientation influence on bond performance, substrates were printed with the bonding surface oriented at 0°, 45° (upskin/downskin) and 90° relative to the base plate, as shown in Figure 1(b). For the 45°-oriented substrate, support structures were employed, as initial trials without support resulted in deformation during subsequent heat treatment. The utilized powder was supplied by GE Additive and has a particle size range of 10–45 µm, fulfilling the ASTM F3001–14[34] specification. Post-processing involved stress relief heat treatment under vacuum at 840°C for 2 hours, followed by EDM Cutting from the build plate and ultrasonic cleaning with deionized water to remove loose particles on the surface.

2.2. Surface treatment

The surface conditions as-built, grit blasted and laser treated were considered in this work. Grit blasting was selected since it is a widely used post-processing method for PBF-LB-manufactured metal parts, whereas laser treatment was investigated as an environmentally friendly alternative to electrochemical processes for creating distinct nanoroughness on metallic surfaces. The specimens in as-built condition were only degreased prior to bonding. Degreasing was conducted for all specimens in this work by ultrasonic cleaning in acetone.

Grit blasting was performed using a Peenmatik 1300 SDK system (iepco, Switzerland) with silicon carbide as the blasting agent, featuring a grain size range of 212–300 µm. Silicon carbide was chosen due to its widespread use as a standard blasting agent in post-processing for AM. The grit blasting process was conducted manually using a 10 mm nozzle and a pressure of 3 bar. The device was operated from a distance of 20 cm, at a blasting angle of approximately 90° and for a duration of about 10 s, ensuring a uniform surface finish was achieved. Post-treatment included ultrasonic cleaning in deionized water to remove abrasive residues, followed by degreasing in acetone.

Laser treatment was conducted under atmospheric conditions on a TRUMPF Trumark Station 5000 marking laser system (TRUMPF, Germany) equipped with a pulsed Nd:YVO4-Laser (TRUMPF TruMark

6350)). This laser system has a maximum average output power of 50 W and operates at a wavelength of 355 nm. The laser settings were adapted to induce pronounced nanoroughness on the surfaces of PBF-LB-Ti6Al4V, without creating unstructured high microroughness through laser splatter. This approach was used to prevent potential deterioration in fatigue performance associated with excessive microroughness and induced tensile residual stresses.[18–21,26] Based on this, the laser treatment was carried out with a power level of 70%, a scan speed of 0.4 m/s, a pulse frequency of 20 kHz and a laser spot diameter of 30 µm. This configuration resulted in a laser energy density of 248 J/cm^2. The laser scanned once over the entire surface, following a horizontal line pattern with a track distance of 30 µm. Degreasing of the specimens was conducted prior to laser treatment. After the laser processing, only cleaning with compressed air was performed to remove residual fine dust from the surface.

2.3. Analysis of surface characteristics

The characterization of the surface topographies was done by Scanning Electron Microscopy (SEM) using a Zeiss ULTRA Plus (Carl Zeiss, Germany) field emission scanning electron microscope. A Secondary Electrons detector (SE2) was primarily used, with the accelerating voltage set to 1.0 kV. For fracture surface analysis an In-Lens detector was additionally utilized to better differentiate between metal and adhesive residues on the surfaces. Furthermore, for selected specimens Ion Beam Milling (IBM) was performed using a Hitachi ArBlade 5000 system (12 h at a milling energy of 5 kV). For IBM, small pieces of about 10 × 10 mm were cut from the fractured specimens at the region of interest using a diamond wire-cutting machine. To prevent surface alteration during further preparation, the fractured surfaces were sputtered with gold. The specimens were then bonded to a sample carrier and ground to the final dimensions. In addition, Confocal Laser Scanning Microscopy (CLSM) was used during fracture analysis to detect fractured particles on the PBF-LB surfaces. The CLSM images were captured on a Keyence VK-X3000 (Keyence International, Belgium).

2.4. Adhesive joint preparation and aging

The two-component epoxy adhesive Loctite EA 9396 AERO (Henkel, Germany) was mixed based on a procedure suggested by Frömmel.[35] This involved mixing under a low atmospheric pressure of 30 mbar using a dual asymmetric centrifugal mixer. The low-pressure process significantly minimizes the presence of defects in the adhesive, such as entrapped gas bubbles, which particularly have a negative influence on fatigue behavior.[35] Afterwards, the degreased substrates were bonded

using a fixture designed for SLJ specimens. To prevent butt joint bonding and minimize the formation of adhesive chamfers, PTFE strips were inserted into the grooves at the overlap ends (Figure 1). Moreover, weight blocks were utilized to ensure sufficient contact pressure during curing. Based on recommendations in,[36] curing was done at 66°C for an extended duration of 80 min. Preliminary temperature control measurements with PT-sensors were conducted to ensure that the target temperature was maintained for at least 60 minutes within the bondline. After curing, excess adhesive on the sides was removed using sandpaper. Due to the highly structured nature of the PBF-LB surfaces, the adhesive bond thickness of the SLJ specimens varied along the overlap approximately between 0.1 and 0.2 mm.

To assess the durability of the SLJs under environmental conditions, a subset of the bonded specimens was immersion aged for 30 days at 60°C in deionized water. This aging process was defined by Frömmel[35] for aluminum/aluminum single-lap joints with similar specimen dimensions and the same adhesive. It was demonstrated that the specified aging duration is sufficient for water diffusion into the bondline, ensuring effective aging of the joints. Consequently, this aging process was applied in the present work.

2.5. Mechanical testing

Quasi-static SLJ-testing was conducted based on DIN EN 2243–6[33] using a Zwick Z150 (ZwickRoell, Germany) universal testing machine. The specimens were mounted using a cardanic suspension to ensure moment-free force application. Testing was carried out under nominal environmental conditions with a displacement rate of 1 mm/min. For strain measurement within the bondline, the DIC system Q400 (Limess GmbH, Germany) was used. Initially, 3D-DIC measurements were conducted with a two-camera setup to check for possible out-of-plane displacement during testing. The setup included 12 Mpx cameras with a spatial resolution of 4096×3000 pixels, paired with macro lenses (80 mm focal length) and distance rings to adjust the measurement area to around 14×10 mm. As shown in Figure 2, one camera (A) was aligned directly perpendicular to the measurement surface, while the other (B) was positioned at a 30° angle. Illumination was provided by three LED lights. The speckle pattern for DIC was created by first applying a base layer of black acrylic spray paint, followed by white speckles using an airbrush spray gun. The 3D-DIC measurements showed that the maximum out-of-plane displacement occurred close to specimen failure and amounted to approximately 0.05 mm, which would cause a strain error of 0.015% in the 2D-DIC measurements. Given this small error, subsequent evaluations within the bondline could be

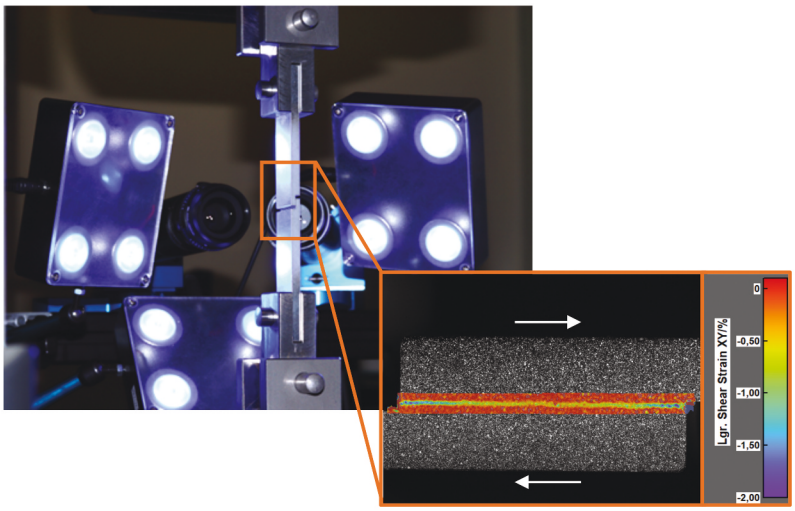

Figure 2. DIC setup for SLJ-testing.

conducted using only the straight camera (A). Following this procedure ensured that the 2D-DIC measurements were not affected by any out-of -plane displacements induced by the test setup. The single-camera setup with straight alignment provides the best camera focus of the bondline, which allows a fine discretization with DIC. Here a facet size of 25 pix and a grid spacing of 9 pix was applied, resulting in a resolution of 83 µm per facet. The adhesive layer was therefore discretized with at least one facet over its thickness.

Fatigue testing was carried out on a servo-hydraulic testing machine using a sinusoidal loading with a frequency of 10 hz and a load ratio of $R = 0.1$. The applied maximum stress was set depending on the quasi-static tensile shear strength. Similar to the quasi-static tests, specimen mounting in the testing machine was done using a cardanic suspension. For evaluating the crack growth, the described DIC setup was used. The DIC system functionality to trigger image acquisition at the maxima of the analog cyclic force signal enabled precise tracking of the crack growth. The image acquisition rate was adjusted for each specimen according to the expected lifetime. A total image count of 150 images per fatigue test was aimed, which resulted in acquisition rates between 1 image per 50 cycles and 1 image per 3000 cycles. A minimum of four specimens were tested for each surface type in each test case. The investigated test cases comprise quasi-static testing with non-aged specimens, quasi-static testing with hot-wet-aged specimens and fatigue testing with non-aged specimens.

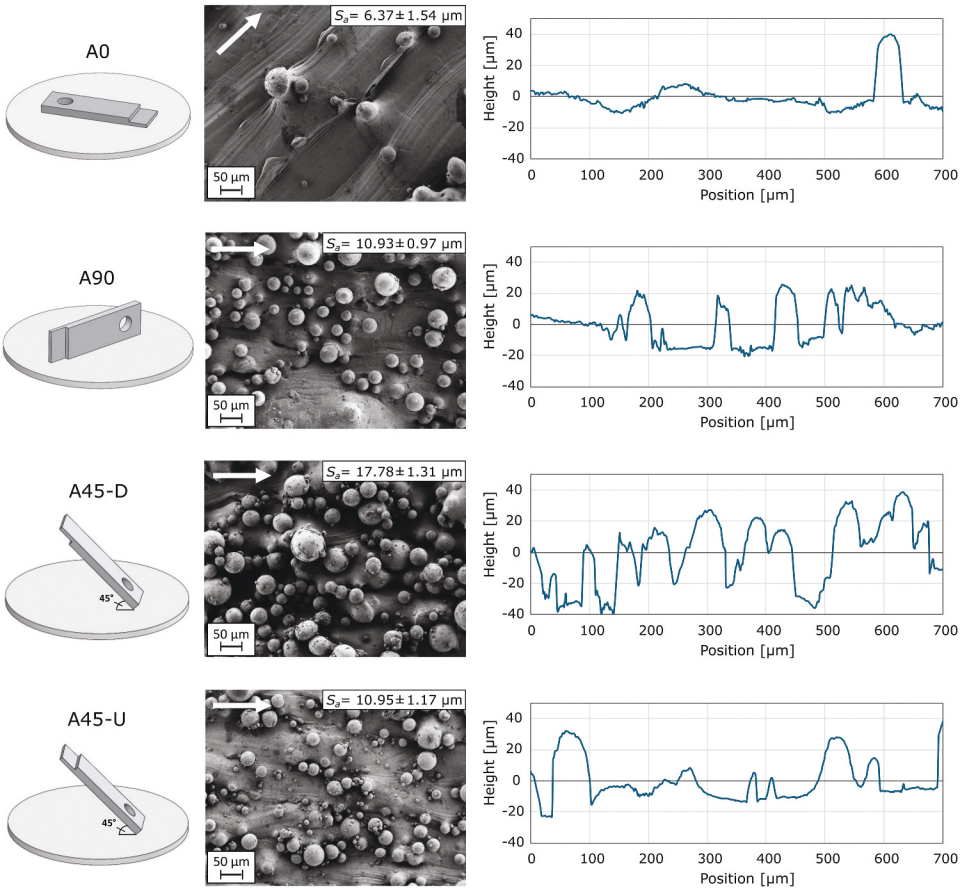

Figure 3. SEM images and height profiles of as-built Ti6Al4V surfaces for the build orientations A0, A45-D/U, A90.

3. Results and discussion

3.1. Surface morphologies

3.1.1. As-built condition

The surface morphologies in the as-built condition were investigated by SEM and CLSM for the build orientations 0° (A0), 45° downskin (A45-D), 45° upskin (A45-U) and 90° (A90). In Figure 3, SEM images are shown for each build orientation, alongside representative surface height profiles and the roughness value S_a obtained from CLSM. The laser scanning direction is depicted in the SEM images. In the as-built condition, the surfaces are mainly characterized by varying numbers of partially melted powder particles. These particles increase the surface area for adhesive bonding and serve as interlocking features.[5,37] Only very few particles are present on the A0 surface, which reflects in a relatively even height profile. In contrast, the A45-D surface is covered with the highest concentration of particles, resulting in a topography

with significant height variation. The attached particles on the A45-D surface are further superimposed with a wavy surface profile, caused by stair-step structuring due to the layer-wise manufacturing.[38,39] The A45-U and A90 surfaces display an intermediate number of attached particles, with large particle-free areas.

In the as-built condition, no distinct nanoscale roughness was observed on the titanium surfaces. Poor bonding behavior is therefore expected in areas with a low number of particles. This lack of nanoroughness on as-built surfaces was also identified in a previous study, where the same build orientations were evaluated for PBF-LB-Ti6Al4V specimens manufactured on a Concept Laser M2 printer.[7] In this investigation, it was demonstrated that commonly used parameters such as the average roughness S_a (arithmetical mean height) or macroscopic contact angles do not correlate with tensile bond strength. To assess the bonding capability of a surface, emphasis should therefore be on analyzing the surface features, particularly the roughness scales. Moreover, it was shown that the as-built PBF-LB-Ti6Al4V surfaces exhibit good to very good macroscopic wettability, which is a necessary requirement for achieving high adhesion strength.

3.1.2. Surface-treated condition

As in a previous study,[7] surface treatment was conducted for the build orientations A0 and A90. This allowed to evaluate the influences on a surface with low and intermediate number of attached particles. The highly structured A45-D surface was not investigated for surface treatment, since it was expected to already provide high adhesive bond strength in as-built condition. A grit blasted surface is exemplarily shown for the build orientation A90 in Figure 4, along with a surface height profile.

Grit blasting produced a more uniform roughness distribution over the surface, but it also removed the attached powder particles. This led to a 36% reduction in the mean roughness value S_a. A small number of blasting agent residues, in the form of incised silicon carbide particles, were observed on the

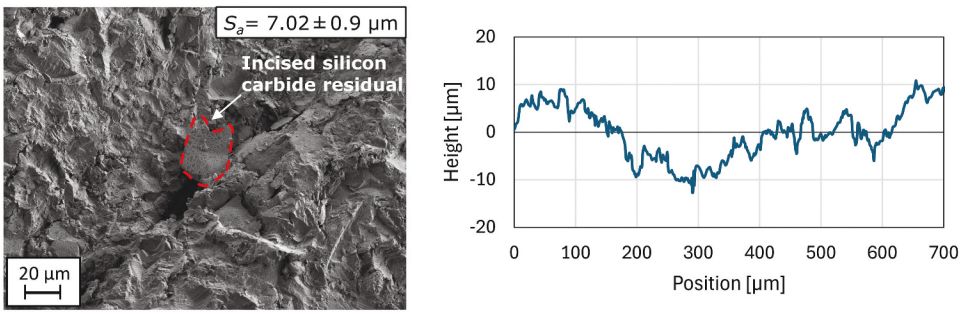

Figure 4. SEM image and height profile of a A90-oriented Ti6Al4V surface after grit blasting.

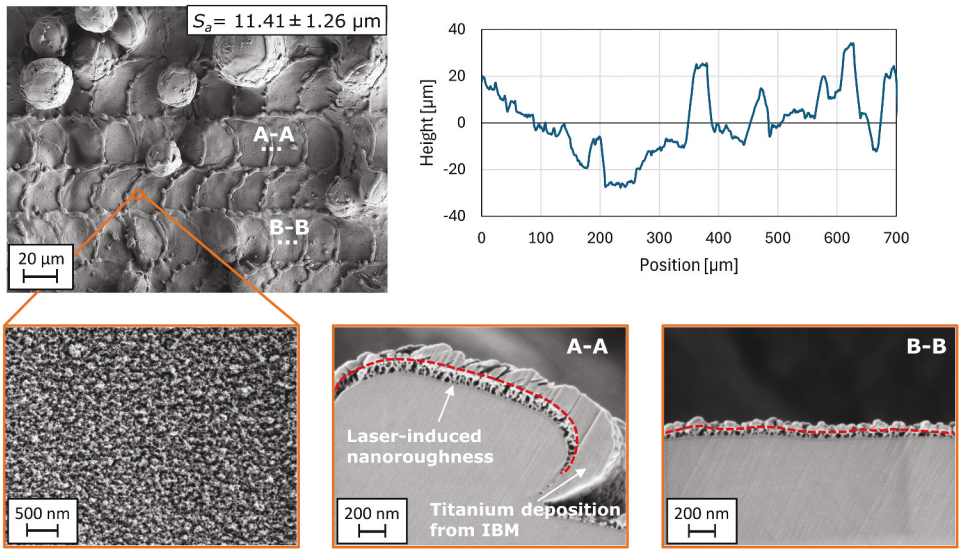

Figure 5. SEM images and height profile of a A90-oriented Ti6Al4V surface after laser treatment. The IBM-prepared cross section views were evaluated at a laser pulse edge (A-A) and laser pulse depression (B-B).

surface. In general, grit blasting mainly modified the microscopic roughness on the surface, without creating a pronounced nanoroughness. No significant differences in surface morphology were observed between A0 and A90 after this treatment.

In contrast, laser treatment allowed to generate roughness on two distinct scales: microroughness and nanoroughness. On the microscale, the laser pulses textured the entire surface, including the attached particles, on a low micrometer range, as illustrated in Figure 5 for the A90 surface. This microroughness is superimposed with a laser-induced nanoporous oxide layer, which is formed by local remelting of the surface under an atmospheric environment. A distinct nanoroughness was also developed on the attached particles surface. Based on investigations in[15,32] with similar laser settings, it can be assumed that the created nanoroughness mainly corresponds to a TiO_2 layer. By filling this nanoporous oxide layer with the adhesive, a high adhesion can be achieved due to the formation of interfacial bonds and mechanical interlocking. In particular, van der Waals interactions become highly effective, if the distance between the substrate surface and the adhesive remains in nanometer scale.[22,40] Wetting of the adhesive in the nanoscale pores is generally unproblematic since wetting is promoted here by high capillary forces.[9] Cross-sectional analysis after IBM revealed that the oxide layer morphology comprises an approximately 10 nm thin barrier layer, above which an open-pored, branched nanostructure with varying thickness and a pore size of approximately 10–40 nm is

formed. The oxide layer thickness generally ranges between 50–100 nm, with higher thickness at the laser pulse edges (Figure 5, A-A) compared to the pulse depressions (Figure 5, B-B). It is important to note that the topmost layer visible in the cross-section images in Figure 5 is not part of the nanoroughness, as it is titanium deposition from the ion milling process. To distinguish this material from the oxide layer, a thin gold layer was applied to the sample before the IBM process. This gold layer is marked with a red line. Similar thicknesses were observed on the surfaces of the attached particles. Moreover, no laser-induced defects or changes in grain structure in the near-surface area of the bulk titanium substrate were found. Laser treatment of the A0 surface resulted in a comparable oxide layer.

In comparison, chromic acid anodizing (CAA)-treated Ti6Al4V substrates, which provide high bond strength and durability, typically have a nanoporous oxide layer with a relatively uniform thickness ranging from 120 to 130 nm on the surface.[9] The laser-induced oxide layer in this work exhibits a more inhomogeneous thickness and is, particularly in the laser pulse depressions, thinner compared to CAA-generated nanoroughness on Ti6Al4V.

To compare the bond performance of laser treated PBF-LB-Ti6Al4V, a combination of the grit blasting and laser treatment process was also considered (GB+LT). This combination creates a surface morphology consisting of the grit blasting textures (Figure 4) superimposed with the laser-induced pulse structures and nanoporous oxide layer (Figure 5).

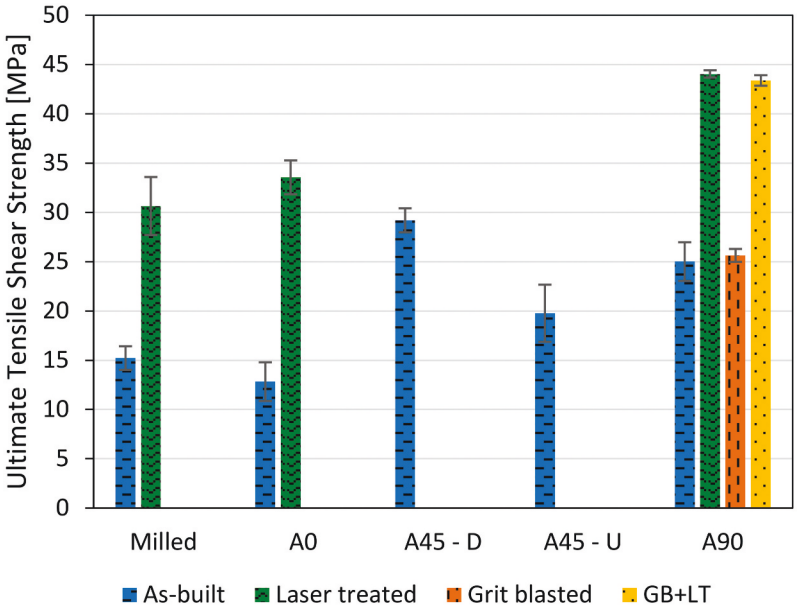

Figure 6. Ultimate tensile shear strengths, shown for the different build orientations in as-built and surface-treated conditions. The results for a milled surface are also shown as a reference.

3.2. Quasi-static loading

3.2.1. Initial adhesive bond performance

The ultimate tensile shear strengths obtained from the quasi-static SLJ-tests of the non-aged specimens are presented in Figure 6. As previously explained, the surface-treated variants were examined for the build orientations A0 and A90. Due to the similar surface morphologies of A0 and A90 after grit blasting, the grit-blasted variants of A0 were excluded from testing. Additionally, results for a milled Ti6Al4V surface are depicted as a reference. It should be noted that the laser treatment of the milled surface was conducted using the same settings, resulting in a comparable oxide layer, as shown in Figure 5.

The tensile shear strengths of the as-built surfaces show a significant dependence on the build orientation. The lowest bond strength, approximately 12.8 MPa, was found for the slightly structured A0-surface, which is comparable to the result of the milled surface without laser treatment. With an increasing number of attached particles on the surface higher bond strengths are reached. Among the as-built surfaces, the highly structured A45-D surface exhibits the highest bond strength of around 29.2 MPa. This enhanced bond strength can be attributed to the large particle accumulations and the wavy structure induced by the stair-stepping effect. The fracture surface of A45-D reveals a mixed-mode failure, with adhesive residues around the particles indicating pronounced interlocking, as shown in Figure 7(a). Compared to the other as-built surfaces, more cohesive failure is present on A45-D. The SEM image was evaluated at the overlap start of the fractured substrate to more clearly illustrate the failure type, as less adhesive residues are present in this region compared to the overlap end. The load direction F is depicted. Due to the significant interlocking on the A45-D surface, a bond strength similar to the milled surface with laser-induced nanoroughness is achieved. This highlights the critical role of mechanical interlocking in tensile shear loading. The

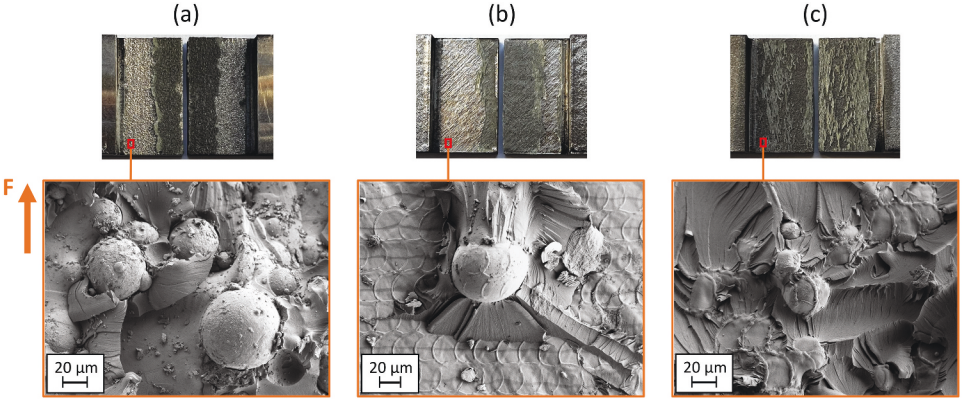

Figure 7. SEM images of the fracture surfaces of quasi-statically tested SLJ specimens with (a) A45-D as-built, (b) A0 laser treated and (c) A90 laser treated surface. The load direction F is depicted.

results show that the tensile shear strength and the extent of cohesive failure correlate with the number of attached particles on the surface. In surface areas with few or no attached particles, adhesive failure is dominant. This indicates that the adhesion strength of the as-built surfaces is mainly governed by mechanical interlocking rather than chemical or dispersive adhesion. The measured tensile shear strengths are therefore primarily determined by the particle density-dependent mechanical interlocking effect.

Grit blasting (GB) of the A90 surface resulted in a similar bond strength compared to the as-built condition, indicating similar effectiveness of the grit blasted surface and the inherent roughness of A90 under tensile shear loading. A significant increase in ultimate tensile shear strength was achieved by laser treatment (LT). For the A0-LT surface, an increase of 162% was observed, resulting in a comparable bond strength to the A45-D surface. This underscores the bonding potential of the inherent roughness of PBF-LB-Ti6Al4V. However, despite the substantial increase in bond strength with laser treatment of the A0 surface, the cohesive strength of the adhesive was not reached. The laser-induced nanoroughness was here insufficient to prevent adhesive failure, as illustrated in Figure 7(b). The interlocking effect of the particles is particularly evident, as demonstrated by an isolated particle on the surface in this SEM image, while no adhesive residues are present in the surrounding laser-structured area. In contrast, laser treatment of the A90 surface resulted in a significantly higher bond strength of around 44 MPa with cohesive failure in the adhesive layer, as shown in Figure 7(c). Furthermore, comparing the results of the A90-LT surface with the grit blasted and laser treated (GB+LT) A90 surface showed similar bond strength and failure mode. This indicates that the as-built A90 surface does not require grit blasting before bonding.

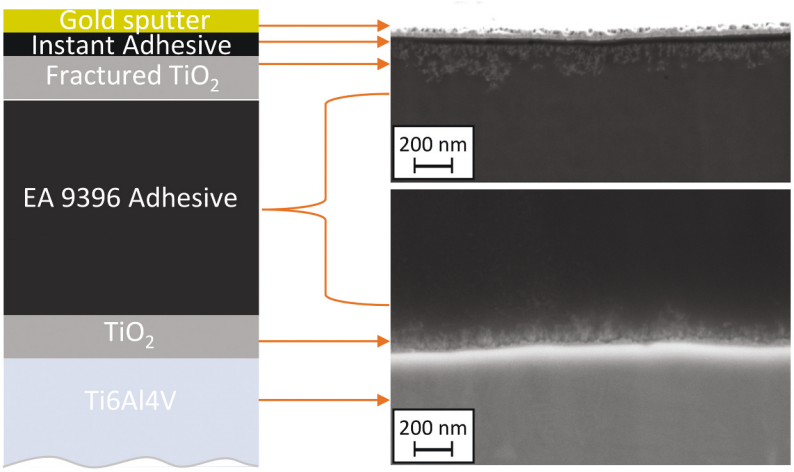

Figure 8. Fracture cross-section prepared by IBM and evaluated by SEM of a quasi-statically tested SLJ specimen with an A0 laser treated surface.

To further investigate the difference in bond strength between laser treated A0 and A90, IBM-prepared cross-sections of fractured specimens were analyzed by SEM. Figure 8 presents the cross-section of an A0-LT specimen after fracture, evaluated at the overlap end. The cross-section reveals two laser-generated nanostructured oxide layers. One belongs to the evaluated substrate, while the other corresponds to the oxide layer fractured from the overlap start region of the opposite substrate side. The adhesive successfully infiltrated the nanoporous roughness, providing enough adhesion strength. However, the cohesive strength of the laser-induced oxide layer was insufficient, which ultimately limited the bond strength. Fracture was found to occur close to the oxide barrier layer. It is assumed that the observed less pronounced nanoroughness in the laser pulse depressions caused failure initiation. Further optimization of the laser settings is therefore necessary. Fracture within the oxide layer also occurred for the milled surface after laser treatment (Milled-LT). A common factor between the A0-LT and Milled-LT surfaces is the absence of a significant microroughness.

In case of the A90-LT surface, no fracture of the oxide layer was found on either substrate side. Figure 9 shows that even in an area with a very thin oxide layer of approximately 50 nm, cohesive fracture does not occur. This can be attributed to the influence of the attached particles, which contribute to load-bearing through interlocking. As a result, the oxide layer experiences less stress, preventing fracture within the layer. This finding demonstrates how microscopic interlocking features can reduce the loading on laser-induced nanoporous roughness, thereby preserving the integrity of the adhesion mechanism. Therefore, the combination of the inherent microscopic interlocking features of PBF-LB-Ti6Al4V surfaces with a distinct nanostructured oxide layer appears to be a promising approach for achieving high adhesive bond performance with AM parts.

To further investigate the adhesive bond performance, the elastic limit was evaluated from the stress-strain curves obtained from SLJ-testing. The term

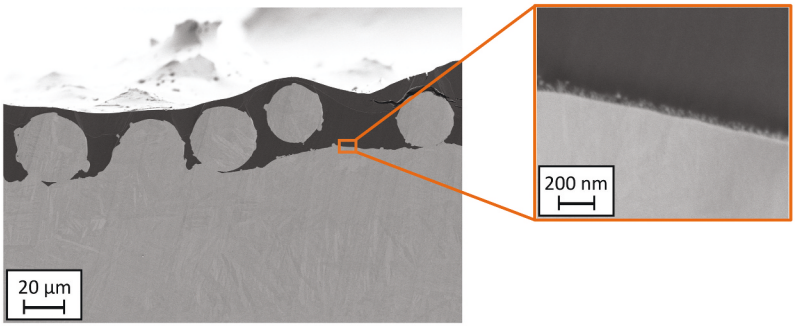

Figure 9. Fracture cross-section prepared by IBM and evaluated by SEM of a quasi-statically tested SLJ specimen with an A90 laser treated surface.

"elastic limit" is used here instead of "yield strength", because the initiation of inelastic deformations is caused for most of the investigated surfaces due to insufficient interfacial bond strength, which is not a material property. The elastic limit was evaluated since significant inelastic deformation was observed in the adhesive and because of its importance in the structural design process. Moreover, it is utilized here as an indicator for premature failure in the joint. For determining the elastic limit, stress-strain curves were calculated using mean stress and shear strain values. The mean shear strain values were determined by averaging the strain distribution, measured via DIC, along the bondline. It is important to note that DIC captured the macroscopic deformation behavior of the adhesive bond, meaning that microscopic effects, such as local plastic deformations around surface asperities, are not considered in detail. The resulting elastic limits are given for the different surface morphologies in Figure 10.

The elastic limits are between 31–66% lower than the ultimate strengths, showing that a significant load increase takes place during inelastic deformation in the adhesive bond. This is caused by the pronounced elastoplastic material behavior of the adhesive and by the load redistribution in the SLJs during damage progression, as observed with DIC. Upon reaching high strain at the overlap ends, progressively more load is transferred through the initially very low loaded inner region.

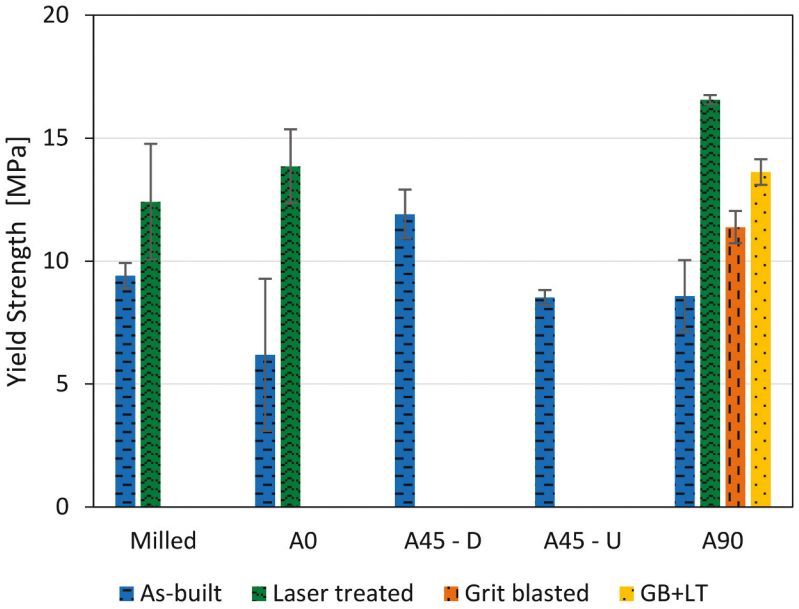

Figure 10. Elastic limits of quasi-statically tested SLJ specimens, shown for the different build orientations in as-built and surface-treated conditions. The results for a milled surface are also shown as a reference.

The relations between the elastic limits achieved with the different surface types are qualitatively similar to the ultimate strength results. For the A90-LT surface, macroscopic inelastic deformation starts due to yielding in the adhesive at the overlap ends at 16.6 MPa. This elastic limit is considerably higher than for the other laser treated surfaces. One possible reason for the lower elastic limit achieved with the Milled-LT and A0-LT surface is the early local fracture of the oxide layer at the overlap ends, due to insufficient adhesion strength. In case of the A90-GB +LT surface, fracture within the oxide layer did not occur. Here, the lower elastic limit could be due to the absence of particle-induced interlocking within the adhesive. Moreover, a low (A0) to intermediate (A90/A45-U) number of attached powder particles on the surface, without a distinct nanoroughness, was found to result in low elastic limits. In such surface morphologies, failure is likely to initiate in areas with no attached particles, leading to macroscopic inelastic deformation at relatively low loads. If large particle accumulations are present, as seen for A45-D, the elastic limit is comparable to the Milled-LT surface. This indicates again a similar effectiveness of distinct nanoroughness and pronounced particle-induced interlocking in enhancing tensile shear loading performance.

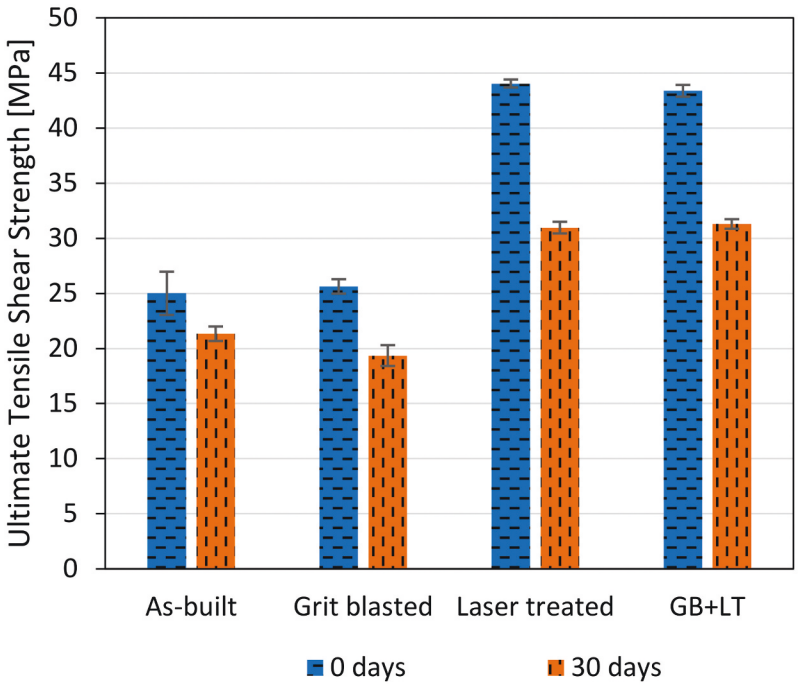

Figure 11. Hot-wet aging influence on ultimate tensile shear strength shown for the A90 build orientation.

3.2.2. Hot-wet-aged

The environmental durability of the adhesive joints was investigated exemplarily for the A90 surfaces, due to the limited number of specimens available. Before testing, the hot-wet-aged specimens were re-dried to eliminate the effect of increased ductility in the adhesive due to water diffusion.[40] The ultimate tensile shear strengths before and after aging are compared in Figure 11.

In all cases, the tensile shear bond strength was reduced due to hot-wet aging. For the grit blasted surface, the decrease in bond strength was slightly higher than for the as-built surface. A more pronounced reduction of 28–30% was observed for the laser treated surfaces. Moreover, evaluating the elastic limits of the aged specimens also revealed a significant reduction of 40–71%. SEM-analysis of the fracture surfaces of the laser treated specimens showed that the failure mode switched from cohesive failure to mixed-mode failure after hot-wet aging. This is illustrated in Figure 12 for the A90-LT surface evaluated at the overlap start region. The same failure mode was observed on the entire overlap region.

Cohesive failure in the adhesive is predominantly present around the edges of the laser pulse imprints, due to the microscopic surface topography and the more distinct nanostructured oxide layer in these areas. However, in the inner regions of the laser pulse imprints, areas with a very thin layer of adhesive residues were found that are adjacent to adhesive-free regions, as illustrated in the image taken with the In-Lens detector (Figure 12(b)). This indicates that the adhesion strength was insufficient in the laser pulse depressions, which corresponds to areas with a less distinct laser-induced oxide layer (Figure 5).

Cross-sectional analysis of a hot-wet-aged A90-LT specimen revealed that fracture of the laser-induced oxide layer occurred (see Figure 13). In the upper area of the cross-section, the fractured oxide layer from the opposite substrate

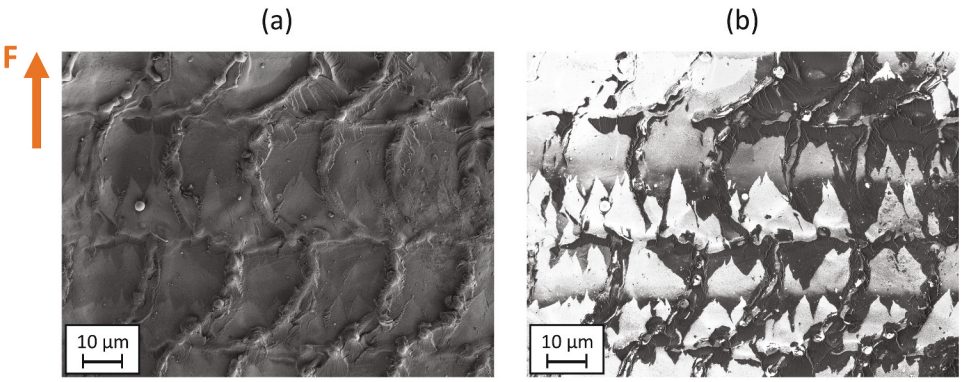

Figure 12. SEM images of the fracture surface of a hot-wet-aged and quasi-statically tested SLJ specimen with an A90 laser treated surface analyzed with (a) SE2 and (b) In-lens detector. The load direction F is depicted.

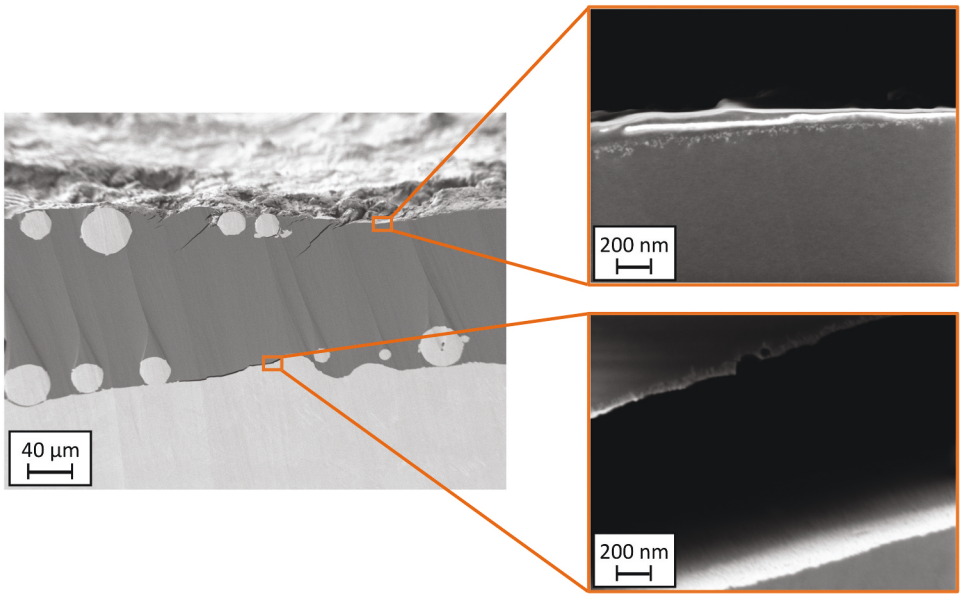

Figure 13. Fracture cross-section prepared by IBM and evaluated by SEM of a quasi-statically tested SLJ specimen with an A90 laser treated surface, after hot-wet aging.

is visible, while partial fractures of the titanium oxide were also found on the evaluated substrate side. Since no fracture of the laser-induced nanoroughness was observed in the non-aged condition of the A90-LT specimen, it is evident that the applied hydrothermal aging process deteriorated the structural integrity of the oxide layer. It is known that in presence of moisture, the cohesive strength of a nanostructured oxide layer can be reduced.[9,41] While this phenomenon is well known for aluminum-epoxy bonds, titanium adherends typically exhibit stable behavior under moderate temperature and humidity conditions.[9] However, prolonged hydration can lead to hydrolytic degradation and swelling of the nanostructured oxide layer, resulting in internal stresses that contribute to micro-cracking.[42] Löbbecke et al.[30] showed that a surface morphology with a pronounced open-pored, branched nanostructure is essential for achieving long-term stable adhesive bonds. The laser-induced nanoroughness created in this work fulfills this requirement, but the inhomogeneous thickness formation on the surface is assumed to cause premature failure of the titanium oxide layer. Further optimization of the laser treatment process is necessary to create a more uniformly distributed or stronger oxide layer. Alternatively, a sol-gel and primer application could help to improve the bond durability, as demonstrated in[6] for PBF-LB-Ti6Al4V adhesive joints subjected to salt-spray aging. Palmieri et al.[43] achieved long-term environmental durability of conventionally manufactured Ti6Al4V bonded joints only after combining laser treatment with sol-gel and primer application. The sol-gel treatment could also be beneficial for high-

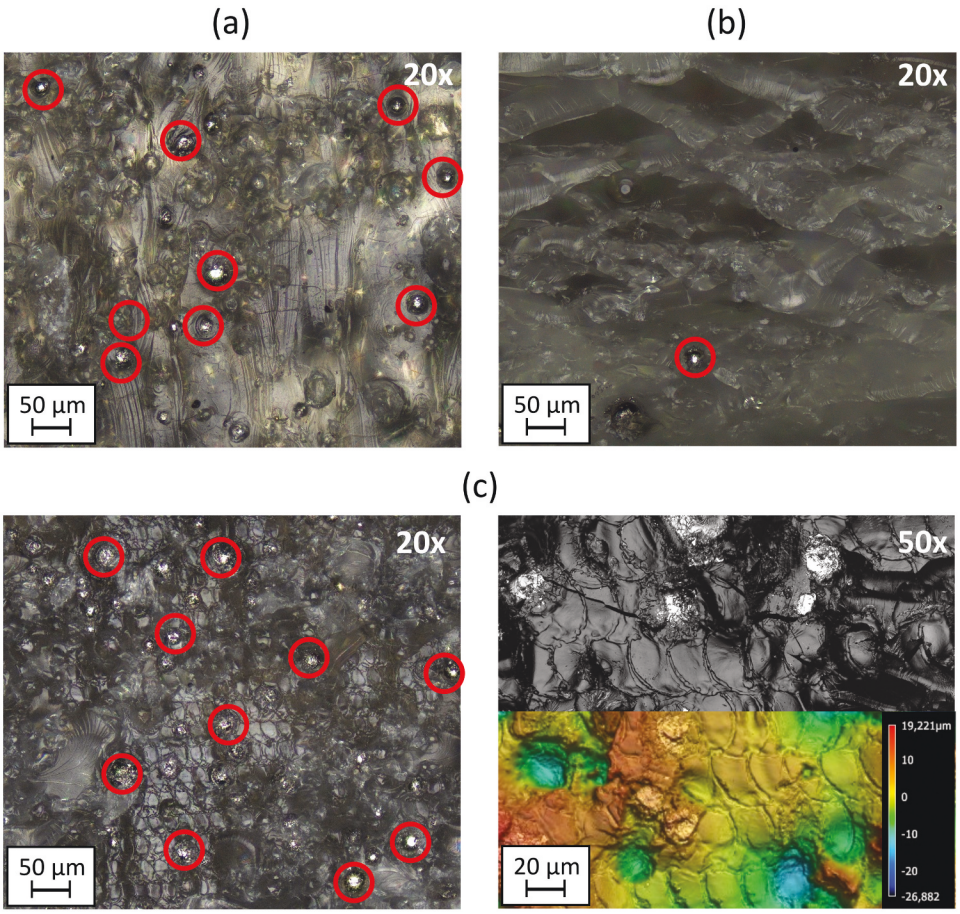

Figure 14. Fracture behavior of the attached powder particles under quasi-static loading, shown by CLSM images for the fracture surfaces of A90 with different surface conditions: (a) as-built, (b) laser treated and (c) laser treated+hot-wet-aged.

temperature applications, where oxide diffusion into the titanium base material can cause voids or microcracks at the metal – oxide interface.[9] The use of corrosion-inhibiting primers is often recommended, even for highly stable oxide layers created by PAA treatments, to further enhance durability.[41,42] If the optimization of the laser process doesn't result in satisfactory durability, a combination with sol-gel and primer application could be a viable alternative to achieve long-term environmental stability.

The upper area of the cross-section in Figure 13 also reveals multiple fractured powder particles, which was rarely observed in the non-aged condition for this surface type. It can be assumed that after failure initiation in the weakened oxide layer, the load was redistributed to the attached particles, leading to an increased number of detached particles. To further assess the fracture behavior of the partially melted powder particles, large areas of the fracture surfaces were examined by CLSM. Figure 14 shows the CLSM images

of A90 surfaces in as-built and laser treated condition. The detached particles are marked.

In the unaged condition, a moderate number of powder particles fractured from the A90 as-built surface under the applied tensile shear loading (Figure 14(a)). However, the majority of the particles remained attached, indicating that they were well connected to the titanium bulk. In contrast, almost no particles fractured on the laser treated A90 surface (Figure 14(b)) due to the nanoroughness contribution to load transfer. This demonstrates how a nanostructured oxide layer can enhance particle-induced interlocking of the adhesive. After hot-wet aging, the number of fractured particles on the A90-LT surface (Figure 14(c)) increased up to a level comparable to the A90 as-built surface (Figure 14(a)) due to the fracture of the oxide layer. It was observed that negative laser pulse imprints on the adhesive fracture surface generally indicate a nanoroughness fracture. It can be concluded, that a cohesively strong nanoroughness is essential to fully leverage the interlocking potential of the attached particles.

3.3. Fatigue loading

To assess the adhesive bond performance under fatigue loading, the investigated surface types were categorized into three groups with similar quasi-static tensile shear strengths, allowing a meaningful comparison. All fatigue tests were conducted with unaged specimens. Moreover, the Milled and A0 as-built surface types were excluded from these tests due to their relatively low adhesion strength. In each group, the maximum stress σ_{max} applied during cyclic loading was set to 40–45% of the mean quasi-static adhesive bond strength, resulting in the stress levels 11.2 MPa, 14.4 MPa and 18.4 MPa. The measured fatigue lifetimes are depicted in Figure 15.

Among the surfaces tested at a stress level of 11.2 MPa, the longest lifetime was reached with the A45-D surface. Compared to the next best surface, A90 grit blasted, a 750% longer lifetime was observed. The combination of a large

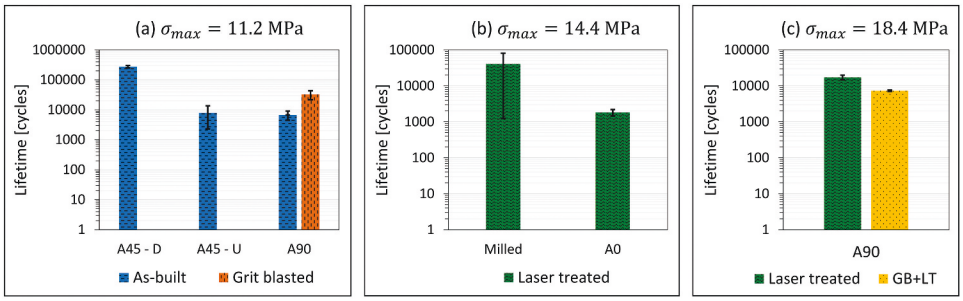

Figure 15. Fatigue lifetimes of SLJs with different surface morphologies, compared at (a) σ_{max}= 11.2 MPa, (b) σ_{max}= 14.4 MPa and (c) σ_{max}= 18.4 MPa.

number of attached particles and the stair-stepping-induced waviness present on the A45-D surface topography appears to be much more effective than the microroughness created by grit blasting for the given fatigue load. This superior performance is likely due to the significant particle-induced interlocking and the large surface area of A45-D. However, surface morphologies with an intermediate number of partially melted particles, such as A45-U and A90, resulted in a shorter lifetime than the grit blasted surface. These results are also reflected in the fracture surfaces, where the lowest amount of adhesive failure was found for the A45-D surface within the given comparison group. Similar to the results from the quasi-static tests, adhesive failure predominantly occurred in areas with few or no attached particles, indicating that these regions offer low fatigue resistance. Thus, the positive effect of the attached particles is significantly enhanced when a high particle concentration is present on the surface.

Comparing the milled and A0 surfaces after laser treatment at a fatigue stress level of 14.4 MPa showed that, on average, the lifetime achieved with Milled-LT is higher. However, considering the high standard deviation observed for Milled-LT, no significant statistical difference is present between both surfaces. The failure mode for both surfaces was fracture of the laser-generated oxide layer, which is consistent with the findings from the quasi-static tests. Very low standard deviations were observed for the A90 surfaces after laser treatment, shown in Figure 15(c). A 130% longer lifetime was achieved with A90-LT compared to A90-GB+LT, underscoring the effectiveness of the combination of attached particles and laser-induced nanoroughness. Evaluating the fracture surfaces showed that these two surface types exhibited a mixed-mode failure. For the A90-LT surface, the primary failure type was fracture of the laser-induced oxide layer, as illustrated in Figure 16(a). Since no fracture of the oxide layer was observed during quasi-static testing for

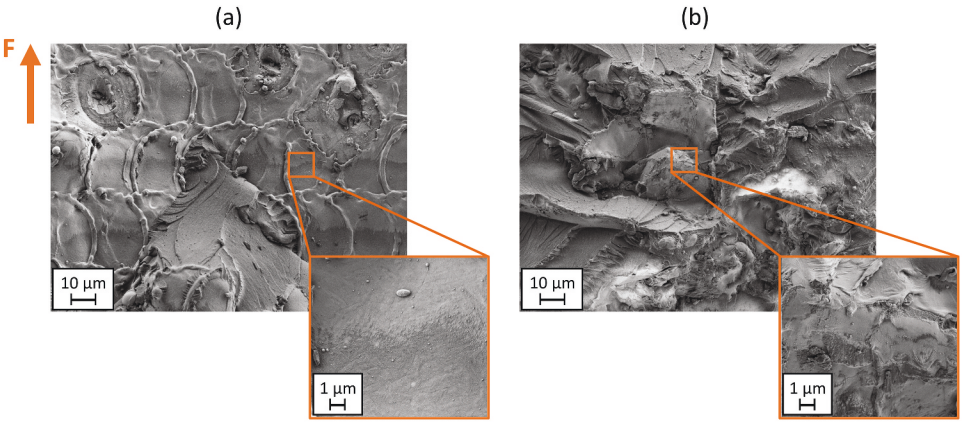

Figure 16. Fracture surfaces of fatigue-loaded SLJ specimens with (a) A90 laser treated and (b) A90 grit blasted+laser treated surface. The load direction F is depicted.

this surface type (Figure 9), it can be assumed that the oxide layer was more severely loaded under the applied fatigue loading condition. On the A90-GB +LT fracture surface, significantly more cohesive failure within the adhesive was found, with only a small portion of the surface showing adhesive failure (Figure 16(b), detail view). This revealed that, for the A90-GB+LT surface, the crack mainly propagated through the adhesive, while on the A90-LT surface, it propagated mostly through the oxide layer, which however resulted in a longer lifetime. Both surface types were treated using the same laser process parameters. No structural changes in the sub-surface area or detrimental effects of laser-induced residual stresses were detected in either case. Moreover, the low number of incised silicon carbide residues on the A90-GB+LT surface did not appear to negatively impact fatigue performance by causing crack initiation. Thus, it can be assumed that the superior fatigue performance achieved with the A90-LT is due to the influence of the attached particles. In addition to interlocking, the particles may also slow down the crack propagation, since it was found that the crack propagates close enough to the surface and is therefore under the direct influence of the particles.

3.3.1. S-N curves

For a more detailed comparison, further fatigue load levels were tested for selected surfaces. The A45-D as-built surface, characterized by its high particle density and the A90-LT surface, with its intermediate number of attached particles and nanoroughness, were chosen due to their remarkable adhesive bond performance. In addition, the particle-free, nanostructured Milled-LT surface was further considered to help differentiate the effects of particle-induced interlocking and nanoroughness on the fatigue behavior. The

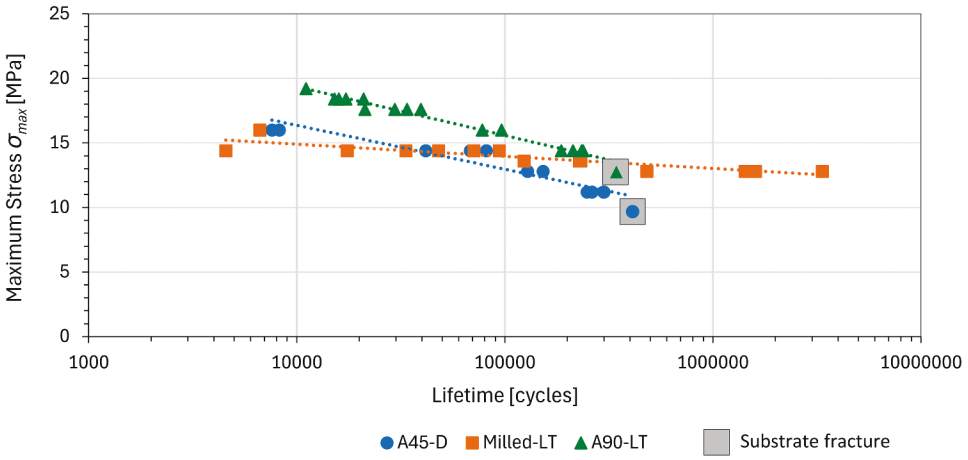

Figure 17. S-N curves of SLJ specimens with A45-D as-built, Milled-LT and A90-LT surface.

comparison is shown in Figure 17, by means of S-N curves in a semi-logarithmic presentation.

In the lifetime range up to 10^5 cycles, the best fatigue performance was reached with the A90-LT surface, while for the other two surfaces similar lifetimes were found. This shows that in the range of low cycle fatigue (LCF) the combination of attached particles and laser-induced nanoroughness provides the highest fatigue resistance. Moreover, it can be stated that both the extensive particle-induced interlocking effect of the A45-D surface and the laser-induced nanostructured oxide layer of the Milled-LT surface show similar effectiveness in LCF. However, above 10^5 cycles (high cycle fatigue (HCF)), bonding with the A45-D surface resulted in shorter lifetimes compared to the Milled-LT surface. Fracture surface analysis revealed that for both surface types, the same failure mode is present as in LCF, namely mixed mode failure for A45-D and oxide layer fracture for Milled-LT. The interlocking effect of the attached particles appears to be inferior in HCF compared to the enhanced adhesion provided by the nanoroughness of the Milled-LT surface. An explanation could be that due to the absence of significant plastic deformation in HCF the crack growth is less influenced by microscopic surface features like the attached particles. It should be noted that for the Milled-LT specimens a significantly higher scattering of the lifetime is present at each load level, indicating a relatively low reliability of this surface condition. Furthermore, the A90-LT surface shows in HCF also a higher fatigue resistance than Milled-LT. It appears that the difference between these two surfaces becomes lower with decreasing load level. This supports the observation that the fatigue behavior in HCF is mainly improved by the nanoroughness rather than by the attached particles. Failure of A90-LT in HCF occurred similarly to LCF due to fracture of the oxide layer. Moreover, the evaluation in HCF was limited since in a certain load range, depending on the surface type, fracture in the bulk titanium substrate occurred before the adhesive bond failed. This was caused by the bending moment present in SLJ-testing.[44] Locus of the failure was at the edge of the stepped specimen geometry, perpendicularly to the load axis. A similar failure mode was observed in[35] at certain fatigue load levels for aluminum-aluminum single-lap joints with flat plate specimens. In the present work, a single step-lap joint geometry was used to reduce the bending moment load at the overlap ends. This approach was effective for the milled specimens, as no fracture occurred in the metallic substrate. Therefore, it is assumed that the surface roughness at the edge was the primary cause of the substrate failure.

3.3.2. Crack growth

The surface morphology influences on crack growth during fatigue loading were investigated by DIC measurements. The main objective was to further

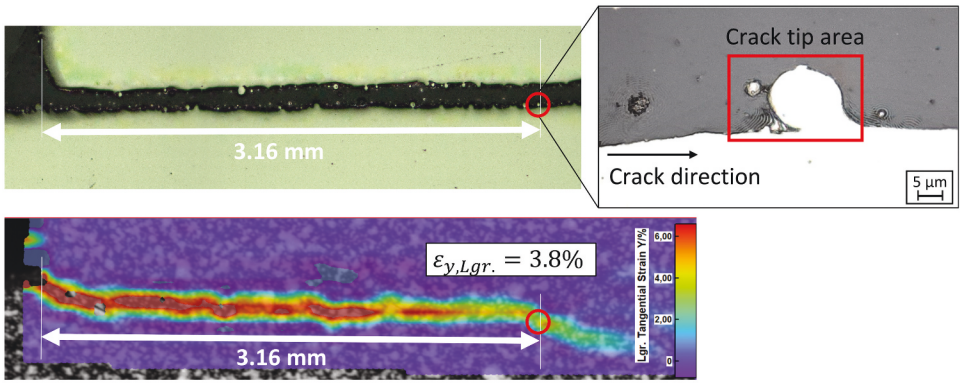

Figure 18. Correlation between crack tip position determined by CLSM and peel strain ε_y measured by DIC.

evaluate the influence of attached particles, nanoroughness and their combination on the fatigue behavior. First, a correlation between the crack tip position and the strain measured by DIC was established. A fatigue test was stopped after a certain number of cycles prior to bond failure. The cross-section of the adhesive joint was subsequently polished and analyzed by CLSM to determine the crack tip position. As shown in Figure 18, the crack tip was located in the vicinity of a particle. The crack length was then correlated with the peel strain ($\varepsilon_{y,Lgr.}$) calculated by the DIC system. The peel strain was used since it is suitable for characterizing crack opening. It was found that a peel strain of 3.8% correlates with the crack tip position. Considering that previous tensile tests of bulk adhesive specimens (EA 9396) resulted in a fracture strain of 3.9%, the determined value appears to be reasonable.

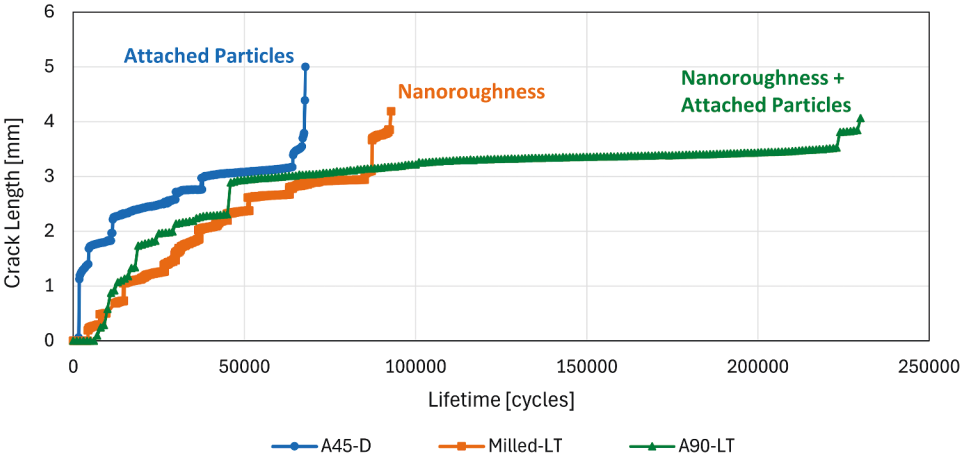

Figure 19. Crack growth of fatigue-loaded SLJs with different surface morphologies, tested at σ_{max}= 14.4 MPa.

In the SLJ specimen, cracks initiate at the overlap ends, resulting in two macroscopic crack paths. In the following, the crack growth results are shown for one crack path, since similar observations were made for both crack fronts. A comparison of the crack growth was conducted for the three detailly investigated surfaces A45-D, Milled-LT and A90-LT. This comparison is shown exemplarily for the maximum stress level of 14.4 MPa, illustrated in Figure 19. Crack initiation occurred already after a few thousand cycles for all three surfaces. No significant differences in crack initiation lifetime were observed between the surfaces, indicating that the varying roughness scales present on these surface morphologies do not cause substantial differences in crack initiation in the LCF regime. Despite the small differences, the results show that the crack initiation lifetimes correlate with the quasi-static bond strengths of the surfaces. It is important to note that none of the considered surfaces has pronounced sharp structures on the microscale that could promote crack initiation.

The overall lifetime was mainly determined by the crack propagation behavior. In the initial phase, the crack propagates significantly faster in case of A45-D, while a similar crack growth rate is observed for Milled-LT and A90-LT. Following this initial phase, the crack propagation rate gradually decreases for all three surfaces until a phase of minimal crack growth occurs. Upon reaching a surface-dependent critical total crack length, unstable crack growth initiates, leading to rapid fracture. Initiation of unstable crack growth occurs much earlier for A45D and Milled-LT than for A90-LT, correlating with the quasi-static bond strength reached with the respective surface morphology. Fracture analysis revealed that, in rare cases, microcracks may form around the attached particles on the surface, which propagate only a short distance before halting. Particle-induced negative effects on the crack growth were therefore not found in the LCF regime.

The positive influence of the attached particles on fatigue behavior can be mainly attributed to their mechanical interlocking effect, which not only increases overall bond strength but can also cause crack paths to be more tortuous, as cracks are forced to propagate around the particles. In addition, considering the pronounced plastic material behavior of the EA9396 adhesive and the applied high fatigue load, it can be assumed that the particles cause local plastic deformations in the adhesive, leading to energy dissipation and thereby reducing the amount of energy available to drive crack propagation. On the other hand, the contribution of the laser-induced nanoroughness to the adhesion strength is primarily based on the significant increase of surface area, allowing interfacial bonds to form and mechanical interlocking of the adhesive in the nanostructures. To combine the advantages of both attached powder particles and laser-induced nanoroughness, a hierarchical surface morphology was created, as seen in the A90-LT surface. With this surface the gradually slowed crack propagation was maintained significantly longer due to the given higher adhesion strength. The

described crack growth behavior was also observed similarly at a higher fatigue load. However, for load levels in the HCF regime, differences in crack initiation and propagation were found between the A45-D and Milled-LT surfaces. The crack initiation and growth were significantly slower in case of Milled-LT. A possible explanation is that the large surface area created by the nanoroughness is particularly effective in reducing stress concentrations, which is crucial under the predominantly elastic loading in HCF. In contrast, the absence of significant plastic deformations in HCF reduces the effectiveness of the attached particles.

4. Conclusions

The surface morphology influences of PBF-LB manufactured Ti6Al4V parts on adhesive bond performance were investigated for different build orientations and surface conditions. The bond strength and fatigue resistance were studied for tensile shear loading, while a hot-wet aging process was applied to assess the bond durability. The main results of this study can be summarized as follows:

- The build-orientation-dependent number of partially melted particles on the as-built surfaces correlates with the tensile shear strength and fatigue life of the adhesive bond.
- Grit blasting the PBF-LB-Ti6Al4V surfaces resulted in a similar bond performance to that of an as-built surface with an intermediate number of attached particles (A90).
- A significant improvement in bond strength and fatigue resistance was achieved by laser treatment, which created a hierarchical surface morphology consisting of the inherent attached powder particles of the PBF-LB process and a laser-induced nanoporous oxide layer. The influences of these surface features on the adhesive bond can be described as follows:
- The partially melted particles cause mechanical interlocking at the microscale and provide an increased surface on which the nanoroughness can be formed. Moreover, under fatigue loading, the particles can cause energy dissipation due to local plastic deformations in the adhesive, which slows down crack propagation in LCF.
- The laser-induced nanoroughness contributes to a significantly increased overall surface area, enhances nanoscale interlocking and improves fatigue behavior in both LCF and HCF.
- Interactions between the attached particles and the laser-induced oxide layer were determined. An increasing number of particles can prevent fracture of the oxide layer, thereby enabling cohesive failure in the adhesive layer. This was observed for the laser treated A90 surface (A90-LT) under quasi-static loading, whereas oxide fracture occurred for A0-LT due to the lower number of particles on the surface. Furthermore, it

was demonstrated that a cohesively strong nanoroughness allows more particles to remain attached to the surface, thus enhancing microscale interlocking.

- In LCF, a comparison of the fatigue lifetimes between a surface with a high number of attached particles (A45-D) and a particle-free, nanostructured surface (Milled-LT) revealed that the partially melted particles and the laser-induced nanoroughness are similarly effective in the adhesive bond.
- In HCF, lower fatigue lifetimes were found for A45-D compared to Milled-LT since the particle-induced interlocking effect diminishes at low loads due to the absence of significant plastic deformations. This lower effectiveness of the attached particles in HCF is also reflected in a faster crack initiation and propagation for A45-D.
- Hot-wet aging resulted in considerably reduced bond strengths, showing that the investigated surface morphologies lack sufficient environmental durability. For the laser treated surfaces, failure occurred due to fracture of the nanostructured oxide layer, which was mainly observed in the laser pulse depressions.
- SEM-analysis of IBM-prepared cross-sections of laser treated specimens revealed that the created nanoroughness was less distinct in the laser pulse depressions compared to the laser pulse edge regions. Therefore, it is assumed that the inhomogeneous thickness formation of the oxide layer caused its cohesive failure, observed after hot-wet aging and also under fatigue loading.
- Further optimization of the laser treatment process is necessary to create a more uniformly distributed or stronger oxide layer. Combinations with sol-gel and primer application could also be viable options to achieve environmental durability.

Acknowledgments

This work is part of the research project BLANCA, which was funded by the Bavarian Ministry of Economic affairs, Regional development and Energy (StMWi) within the program BayLu-25. We thank the project partner Modell- und Formenbau Blasius GERG GmbH, for printing the substrates. The authors also thank the Institute of Materials Science (University of the Bundeswehr Munich) and the Bundeswehr research institute WIWeB for providing access to their laboratory equipment.


Sponsored by
Bavarian Ministry of Economic Affairs,
Regional Development and Energy

Disclosure statement

No potential conflict of interest was reported by the author(s).

Funding

This work was supported by the Bavarian Ministry of Economic affairs, Regional development and Energy.

Data availability statement

The data that support the findings of this study are available from the corresponding author upon request.

References

[1] Koch, C.; Richter, J.; Vollmer, M.; Kahlmeyer, M.; Niendorf, T.; Böhm, S. Adhesively Bonded joints in Components Manufactured via Selective Laser Melting. *Proc. Inst. Mech. Eng. Part C: J. Mech. Eng. Sci.* 2021, *235*(3), 518–526. DOI: 10.1177/0954406220959376.

[2] European Cooperation for Space Standardization. *Space Engineering Adhesive Bonding Handbook ECSS-E-HB-32-21A*; ESA Requirements and Standards Division: Noordwijk, 2011.

[3] Marques, A. C.; Mocanu, A.; Tomic, N. Z.; Balos, S.; Stammen, E.; Lundevall, A.; Abrahami, S. T.; Günther, R.; de Kok, J. M.; de Freitas, S. T. Review on Adhesives and Surface Treatments for Structural Applications: Recent Developments on Sustainability and Implementation for Metal and Composite Substrates. *Materials* 2020, *13*(24), 5590. DOI: 10.3390/ma13245590.

[4] Campbell, F. C., Ed. Adhesive Bonding and Integrally Cocured Structure: A Way to Reduce Assembly Costs Through Parts Integration. In Manuf Process Adv Compos. Elsevier S: Amsterdam, 2004; pp 241–301. DOI: 10.1016/B978-1-85617-415-2.X5000-X .

[5] Nguyen, A. T.; Brandt, M.; Orifici, A. C.; Feih, S. Hierarchical Surface Features for Improved Bonding and Fracture Toughness of Metal-Metal and Metal-Composite Bonded Joints. *Int. J. Adhes. Adh* 2016, *66*, 81–92. DOI: 10.1016/j.ijadhadh.2015.12.005.

[6] Ardila-Rodriguez, L. A.; Rans, C.; Poulis, J. A. Effect of Surface Morphology on the Ti–Ti Adhesive Bond Performance of Ti6Al4V Parts Fabricated by Selective Laser Melting. *Int. J. Adhes. Adh* 2021, *110*, 102918. DOI: 10.1016/j.ijadhadh.2021.102918.

[7] Ertürk, E.; Musil, B.; Diez, G.; Felber, C.; Höfer, P. Surface Morphology Influences of PBF-LB Manufactured Ti6Al4V Parts on Adhesive Bond Strength—Investigation of As-Built and Surface-Treated Conditions. *Prog. Addit. Manuf.* 2023, *8*(4), 719–731. DOI: 10.1007/s40964-023-00450-7.

[8] Nusom, Y.; Srimanosaowapak, S.; Uthaisangsuk, V. Effects of 3D-Printing Surface Morphologies on Interfacial Bonding Strength Between Ti–6Al–4V and CFRTP with PMCs Interlayer. *Int. J. Adhes. Adh* 2023, *121*, 103313. DOI: 10.1016/j.ijadhadh.2022.103313.

[9] da Silva, L. F. M.; Öchsner, A.; Adams, R. D., editors *Handbook of Adhesion Technology*; Springer: Berlin, Heidelberg, 2018. DOI: 10.1007/978-3-319-55411-2.

[10] Avinç Akpinar, I. The Effect of Chemical Etching and Nanostructure Additive Epoxy Coating Technique on Adhesion Strength in Aluminum Joints Bonded with Nanostructure Additive Adhesive. *Int. J. Adhes. Adh* 2024, *129*, 103584. DOI: 10.1016/j.ijadhadh.2023.103584.

[11] Avinç Akpinar, I. Effect of Chemical Oxidation Process on Adhesive Performance in Two Component Adhesive with Nano Particle and Nano Fiber Additives. *Eur. Mech. Sci.* 2024, *8*(1), 29–37. DOI: 10.26701/ems.1385552.

[12] Akpinar, S.; Kars, A.; Bayramoglu, S.; Demiral, M. The Influence of Combination of Surface Roughness and Nanostructure of Adhesive on the Strength of Adhesively Bonded Joints. *Int. J. Adhes. Adh* 2024, *133*, 103743. DOI: 10.1016/j.ijadhadh.2024.103743.

[13] Wegman, R. F.; van Twisk, J. *Surface Preparation Techniques for Adhesive Bonding*; William Andrew: Norwich, 2013. DOI: 10.1016/C2012-0-02158-8.

[14] Matz, C. Optimization of the Durability of Structural Titanium Adhesive Joints. *Int. J. Adhes. Adh* 1988, *8*(1), 17–24. DOI: 10.1016/0143-7496(88)90053-X.

[15] Kurtovic, A. Laserinduzierte Nanostrukturierung von Titanoberflächen für das strukturelle Kleben - Einfluss auf die Oberflächenmorphologie, Ermüdungs- und Adhäsionseigenschaften. Dissertation, Universität Paderborn, 2014.

[16] Tseng, S. F.; Chen, Y. S. Surface Microtexturing of Ti-6Al-4V and SS316L Alloys Using High Pulsed Fiber Lasers for Improving the Adhesive Bonded Performance. *Opt. Las. Tech.* 2021, *143*, 107349. DOI: 10.1016/j.optlastec.2021.107349.

[17] Parkes, P. N.; Butler, R.; Meyer, J.; de Oliveira, A. Static Strength of Metal-Composite Joints with Penetrative Reinforcement. *Comp. Struc.* 2014, *118*(250), 250–256. DOI: 10.1016/j.compstruct.2014.07.019.

[18] Naat, N.; Boutar, Y.; Naimi, S.; Mezlini, S.; Da Silva, L. F. M. Effect of Surface Texture on the Mechanical Performance of Bonded Joints: A Review. *J. Adhes.* 2023, *99*(2), 166–258. DOI: 10.1080/00218464.2021.2008370.

[19] de Barros, S.; Kenedi, P. P.; Ferreira, S. M.; Budhe, S.; Bernardino, A. J.; Souza, L. F. G. Influence of Mechanical Surface Treatment on Fatigue Life of Bonded Joints. *J. Adhes.* 2017, *93*(8), 599–612. DOI: 10.1080/00218464.2015.1122531.

[20] Thäsler, T.; Holtmannspötter, J.; Gudladt, H. J. Surface Topography Influences on the Fatigue Behavior of Composite Joints. *Key Eng. Mat.* 2019, *809*, 341–346. DOI: 10.4028/www.scientific.net/KEM.809.341.

[21] Morfini, I.; Goglio, L.; Belingardi, G.; Nassar, S. A. Effect of Autoclave Cure Time and Bonded Surface Roughness on the Static and Fatigue Performance of Polyurethane Film Adhesive Single Lap Joints. *Int. J. Adhes. Adhes.* 2019, *92*(37), 37–43. DOI: 10.1016/j.ijadhadh.2019.03.015.

[22] Gudladt, H. J.; Frömmel, S. A. Fatigue and Fracture Behavior of Adhesive-Bonded Structures in the Light of the Surface Morphology. *Int. J. Adhes. Adh* 2019, *88*, 74–80. DOI: 10.1016/j.ijadhadh.2018.10.016.

[23] Moroni, F.; Musiari, F.; Favi, C. Effect of the Surface Morphology Over the Fatigue Performance of Metallic Single Lap-Shear Joints. *Int. J. Adhes. Adh* 2020, *97*, 102484. DOI: 10.1016/j.ijadhadh.2019.102484.

[24] Bagehorn, S.; Mertens, T.; Greitemeier, D.; Carton, L.; Schoberth, A. Surface finishing of additive manufactured Ti-6Al-4V - a comparison of electrochemical and mechanical treatments; 6th Eur Conf Aerosp Sci; Krakow, Poland, 2015.

[25] Kahlin, M.; Basu, D.; Kerwin, A.; Moverare, J. J.; Ansell, H.; Newton, L.; Smith, B. Improved Fatigue Strength of Additively Manufactured Ti6Al4V by Surface Post Processing. *Int. J. Fat.* 2020, *134*, 105497. DOI: 10.1016/j.ijfatigue.2020.105497.

[26] Taube, A.; Kurtovic, A.; Niendorf, T.; Mertens, T.; Zinn, C.; Schaper, M.; Maier, H. J. Influence of Surface Pre-Treatments on the High-Cycle Fatigue Behavior of Ti–6Al–4V – from Anodizing to Laser-Assisted Techniques. *Int. J. Fat.* 2016, *91*, 195–203. DOI: 10.1016/j.ijfatigue.2016.06.010.

[27] Costa, M.; Viana, G.; Da Silva, L. F. M.; Rdsg, C. Effect of Humidity on the Mechanical Properties of Adhesively Bonded Aluminium Joints. *Proc. Inst. Mech. Eng. Part L: J. Mater. Des. Appl* 2016, *232*(9), 733–742. DOI: 10.1177/1464420716645263.

[28] Bellini, C.; Parodo, G.; Polini, W.; Sorrentino, L. Influence of Hydrothermal Ageing on Single Lap Bonded CFRP Joints. *Frat. Ed. Integrità Strutt.* 2018, *12*(45), 173–182. DOI: 10.3221/IGF-ESIS.45.15.

[29] Clearfield, H. M.; McNamara, D. K.; Davis, G. D. Adherend Surface Preparation for Structural Adhesive Bonding. In Adhesive Bonding, Lee, L., Ed.; Springer: Boston, 1991. DOI: 10.1007/978-1-4757-9006-1_8.

[30] Löbbecke, M.; Bayerbasi, T. J.; Bartsch, M.; Haubrich, J. Role of Surface Structures on Long Term Stability of Adhesive Joints Between Ti–15V–3Cr–3Sn–3Al and Polyether-Ether-Ketone. *Int. J. Adhes. Adh* 2023, *120*, 103282. DOI: 10.1016/j.ijadhadh.2022.103282.

[31] Freund, J.; Lützenkirchen, I.; Löbbecke, M.; Tröster, T.; Haubrich, J.; Delp, A.; Wu, W. F. Transferability of the Structure–Property Relationships from Laser-Retreated Metal–Polymer Joints to Aluminum–CFRP Hybrid Joints. *J. Compos. Sci.* 2023, *7*(10), 427. DOI: 10.3390/jcs7100427.

[32] Specht, U.; Ihde, J.; Mayer, B. Laser Induced Nano-Porous Ti–O-layers for Durable Titanium Adhesive Bonding. *Mat. Sci. Eng. Tech.* 2014, *45*(12), 1116–1122. DOI: 10.1002/mawe.201400360.

[33] Deutsches Institut für Normung e. V. Aerospace Series - Non-Metallic Materials - Structural Adhesives – Test Method – Part 6: Determination of Shear Stress and Shear Strain EN 2243-6. DIN Media: Berlin, 2006. DOI: 10.31030/9663277.

[34] ASTM International. *Standard Specification for Additive Manufacturing Titanium-6 Aluminum-4 Vanadium ELI (Extra Low Interstitial) with Powder Bed Fusion ASTM F 3001:2014*; West Conshohocken, PA: ASTM International, 2014.

[35] Frömmel, S. A. Untersuchungen zum mechanischen Verhalten von Klebverbindungen unter Berücksichtigung von Grenzflächendefekten. Dissertation, Universität der Bundeswehr München, 2013.

[36] Henkel Corporation Aerospace. Loctite EA 9396 AERO Technical Data Sheet. 2013. https://www.aero-consultants.ch/view/data/3285/Produkte/Henkel%20Adhesive/LOCTITE%20EA%209396%20AERO.pdf. (accessed Aug 11, 2024).

[37] Bagnato, T.; Ravindran, A. R.; Mirabedini, A.; Ladani, R. B.; Kandare, E.; Orifici, A. C.; Chang, P.; Wang, J.; Mouritz, A. P. Superior Interfacial Toughening of Hybrid Metal-Composite Structural Joints Using 3D Printed Pins. *Compos. Part A* 2023, *168*, 107479. DOI: 10.1016/j.compositesa.2023.107479.

[38] Ventola, L.; Robotti, F.; Dialameh, M.; Calignano, F.; Manfredi, D.; Chiavazzo, E.; Asinari, P. Rough Surfaces with Enhanced Heat Transfer for Electronics Cooling by Direct Metal Laser Sintering. *Int. J. Heat Mass Transf.* 2014, *75*, 58–74. DOI: 10.1016/j.ijheatmasstransfer.2014.03.037.

[39] Viale, V.; Stavridis, J.; Salmi, A.; Bondioli, F.; Saboori, A. Optimisation of Downskin Parameters to Produce Metallic Parts via Laser Powder Bed Fusion Process: An Overview. *Int. J. Adv. Manuf. Technol.* 2022, *123*(7–8), 2159–2182. DOI: 10.1007/s00170-022-10314-z.

[40] Arikan, E. S. Oberflächenmodifikation von Polyetheretherketon (PEEK) für das strukturelle Kleben in der Luftfahrt. Dissertation, Universität der Bundeswehr München, 2020.

[41] Davis, G. D. Surface Treatment of Aluminum and Titanium: From Basic Research to Production Failure Analysis. *Surf. Interf. Anal.* 1991, *17*(7), 439–447. DOI: 10.1002/sia.740170706.

[42] Rider, A. N.; Arnott, D. R.; Mazza, J. J. Surface Treatment and Repair Bonding. In Aircraft Sustainment and Repair; Butterworth-Heinemann: Oxford, 2018; pp. 253–323. DOI: 10.1016/B978-0-08-100540-8.00007-8.

[43] Palmieri, F. L.; Crow, A.; Wohl, C. J.; Connell, J. W.; Belcher, M. A.; Blohowiak, K. Y.; Zetterberg, A.; Hopkins, J. Further Investigation into the Use of Laser Surface Preparation of TI-6AL-4V Alloy for Adhesive Bonding. Int SAMPE Tech Conf; Seattle, WA, 2014.

[44] Goland, M.; Reissner, E. The Stresses in Cemented Joints. *J. Appl. Mech.* 1944, *11*(1), A17–A27. DOI: 10.1115/1.4009336.